



HAL
open science

Orientation Sensing With a Loop Resonator Based on Its Re-Radiation Pattern

Florian Requena, Nicolas Barbot, Darine Kaddour, Etienne Perret

► **To cite this version:**

Florian Requena, Nicolas Barbot, Darine Kaddour, Etienne Perret. Orientation Sensing With a Loop Resonator Based on Its Re-Radiation Pattern. *IEEE Sensors Journal*, 2023, 23 (3), pp.3159-3172. 10.1109/JSEN.2022.3231342 . hal-04775587

HAL Id: hal-04775587

<https://hal.science/hal-04775587v1>

Submitted on 10 Nov 2024

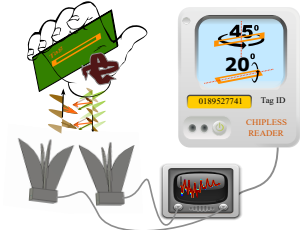
HAL is a multi-disciplinary open access archive for the deposit and dissemination of scientific research documents, whether they are published or not. The documents may come from teaching and research institutions in France or abroad, or from public or private research centers.

L'archive ouverte pluridisciplinaire **HAL**, est destinée au dépôt et à la diffusion de documents scientifiques de niveau recherche, publiés ou non, émanant des établissements d'enseignement et de recherche français ou étrangers, des laboratoires publics ou privés.

Orientation Sensing with a Loop Resonator based on its Re-Radiation Pattern

Florian Requena, *Student Member, IEEE*, Nicolas Barbot, *Member, IEEE*, Darine Kaddour, *Member, IEEE*, and Etienne Perret, *Senior Member, IEEE*

Abstract—This paper presents an analytical model of the radiation pattern of a loop resonator which is frequently used as chipless RFID tags. The radiation pattern of this resonator can be used in practice as a sensor to determine the orientation between the tag and the antenna. Contrary to already implemented chipless RFID angle sensors, the one introduced here allows to extract rotation of the tag or the antenna position in 3D using a novel approach based on the resonator radiation pattern. An analytical model is developed to measure the tag orientation determining both the inclination and azimuthal angle of the tag in spherical coordinates system for both mono-static and bi-static antenna configurations. Uncertainties are studied with Monte-Carlo simulations. Simulations and measurements are performed to validate the orientation extraction and evaluate the performance of the proposed solution. We show that the accuracy of this totally passive and wireless sensor is always below 5° in the measurable range with a maximum error lower than 3° for the mono-static case.



Index Terms—Angular Position sensor, Chipless RFID, Orientation Sensor, Scatterer, Wireless measurement

I. INTRODUCTION

THE possibility of knowing information such as the position or orientation of objects around us will allow the development of new applications and services that adapt their behaviour according to the user's needs and all this in an environment that can evolve over time. For example, a large number of pervasive applications have as input data the orientation of objects [1]. We find this need as well in the case of motion tracking [2], human activity recognition [3], or in gaming where users interact by moving a joystick for example. If we take the example of motion tracking [2], we can mention bottle production lines, on which the bottles can rotate continuously. On this type of line, different operations (such as spray painting or labelling) have to be performed on the moving objects, which requires to know in real time the orientation of the object on which an intervention is needed [4]. To perform this type of task, which is very frequent in practical production lines, it is essential to have information on the orientation of the objects. This information is most often available by using elaborate sensors such as inertial measurement unit, gyroscopes or simply compass. These devices are very well adapted to applications such as the tracking of an aircraft or a missile but are unusable on objects of low value or size as in the example of bottle line production. For this, a solution without battery, with the least possible electrical component is expected. This in particular to lower significantly the unit cost or the environmental

impact. However, these significant constraints mean that this problem is not easy to solve. In the literature, we find works on the use of RFID systems to track the orientation of a batteryless objects [5]. In this case a 3D rotation detection system is proposed where several tags are positioned on the object, and it is the phase difference between each tag that is used to track the orientation of the object. On the application side, it can also be expected that these systems can determine the position of the object in addition to its orientation [1], [4]. For example, in [4], a study was made on the link between the rotation of a UHF RFID tag at a fixed distance and the evolution of the phase measured by the reader. In order to go further in the development of orientation tracking systems always less invasive in terms of electronic component to be added on the objects to be sense, the objective of the present work consists in proposing a solution based on a chipless tag which alone would make it possible to bring an original answer to the problem. The idea is to use a radar reading approach for which a specific resonant scatterer has been introduced to achieve the desired function. The resulting solution is as basic as possible at the label level (a single conductive pattern is used as a scatterer, without any other element). This reduces both the cost of the solution and its carbon footprint. Traditional radar applications allow the detection of a target presence, position and/or velocity. Classical architectures are composed of one or several antennas able to emit an electromagnetic wave towards the target and to receive the backscattered field. Backscattering applications based on this principle are also used for identification and sensing. In such a case, the main difference with traditional radar application is the

The authors are with Univ. Grenoble Alpes, Grenoble INP, LCIS, F-26000 Valence, France.

E. Perret is also with Institut Universitaire de France, Paris, France.

use of a known target that has been designed for encoding an information for identification purposes [6]. The most elaborate approaches of this type are based on the use of labels composed of EM resonators. The signal backscattered by the label will therefore contain the EM fingerprint linked to these resonators. From there, hardware techniques on wave polarization for example or software on signal processing will allow to isolate the signature of the label from that of the environment [7]. Thus, the extraction of resonance frequencies allows us to trace the identifier present on the label. Sensing applications can also be implemented on this principle since the backscattered signal also depends on a large number of physical parameters related to the tag, such as its position, orientation or temperature, to mention only the most studied contributions. Indeed, it has been shown that using a specifically designed radar target and a Vector Network Analyser (VNA), several physical quantities can be sensed wirelessly and without battery such as temperature [8], humidity [9], gas [10] or, permittivity [11]. This information is most often related to variations in the resonant frequencies of the scatterers that can be recorded from the backscattering wave, or to the values of the phase or amplitude of these signals at resonant frequencies [2].

For orientation sensing, most of the studies have been focused on considering the detection of the tag's rotation in the plane perpendicular to the propagation vector using co-polarization [12], [13] or cross-polarization [14]–[17] measurements. All these methods permit to determine the orientation of the chipless tag from the magnitude of the received signal and are often based on a reference measurement which has to be done at the same distance and in a known orientation. It can also be noted that it is possible with a radar approach to detect yaw and pitch change with the help of a dedicated designed transponder [18].

In this paper, a novel approach is introduced to determine the roll orientation of a loop resonator tag, i.e. its inclination and azimuthal angles when considering a spherical coordinate system. This approach is based on an analytical model of the radiation pattern of the loop resonator and is significantly different from the EM polarization based methods described in the literature. The proposed approach is derived to be independent from the reading distance, the loop tag geometry and does not depend on a reference measurement. The paper is organized as follows : Section II presents the loop model and a simplified case where only the azimuth of the tag is investigated. The analytical expression used to extract the tag orientation from the measured S-parameters is introduced. In Section III, simulations are presented to validate this novel method. Section IV illustrates measurements in a controlled and real environment with mono and bi-static antenna configurations. Section V generalizes the problem to the extraction of the azimuth and the elevation of the tag at the same time. Finally, Section VI presents some real environment measurements and Section VII concludes the paper.

II. LOOP MODELING AND AZIMUTHAL ANGLE DETERMINATION

In this section, from the observation of the current distribution on the loop resonator shown in Fig. 1, a simple model based on array antennas is introduced. The coordinate system used in this paper is illustrated in Fig. 1. Note that the loop is positioned in the xOz plane. The objective in this section is to estimate the angle ϕ between the loop and the receiving antenna placed in the xOy plane when the resonator rotates around the z -axis (azimuthal angle). Note that the angle Ω is defined as the angle between the loop and the emitting antenna. The angle α is the angle between both antennas. If a mono-static antenna configuration is used then $\alpha = 0$. Finally, θ is the angle between the z -axis and the direction of propagation of the incident and reflected field (these fields being related to the position of the transmitting and receiving antennas). In other words, it is the inclination (or polar angle) in the spherical coordinate system of reference. Note that in the simplified configuration studied in section 2, this angle is equal to $\pi/2$.

A. Radiation pattern modeling

A rectangular loop, known to have a high Q-factor [19], is considered in this study (see Fig. 1). When impinged by a plane wave along the y direction, significant currents are induced along the small arms of the loop at the fundamental frequency and harmonics. The approach introduced is based on the use of the first two resonance modes of the loop.

Electromagnetic simulation has been done using CST MW to illustrate the surface current distribution at resonance on the loop for the fundamental and first harmonic. These currents are in phase at the fundamental frequency and for odd harmonics while they are in opposition of phase for even harmonics as in Fig. 2. Surface currents are also induced in the top and bottom arms of the loop but they are always in phase opposition. Since the top and bottom arms are close to each others, the radiated field caused by them is nearly cancelled out. For this reason, these currents are not considered in the rest of this paper. As a result, we can model the loop resonator as two small dipoles of length L and spaced $\lambda/2$ apart in the z direction as illustrated in Fig. 3 with λ taken at the fundamental frequency f_1 .

If we consider the two dipoles with the same current I_0 , the total radiated electric field \vec{E}_s is the complex summation of the two electric fields radiated by the two dipoles. This quantity \vec{E}_s can be obtained using the array-factor (AF) from the array-antenna theory knowing the electric field radiated by a single infinitesimal dipole \vec{E}_d as [20] :

$$\vec{E}_s = \vec{E}_d \times AF = \left(j\eta \frac{kI_0 L e^{-jkr}}{8\pi r} \sin(\theta) \vec{e}_\theta \right) \times \left(\frac{\sin(kd \sin(\theta) \cos(\phi) + \beta)}{2 \sin(0.5(kd \sin(\theta) \cos(\phi) + \beta))} \right) \quad (1)$$

where k is the wavenumber, d and β are respectively the distance and the phase difference between the dipoles. I_0 the uniform current flowing through a dipole with length L and r is the distance between the center of the coordinate system

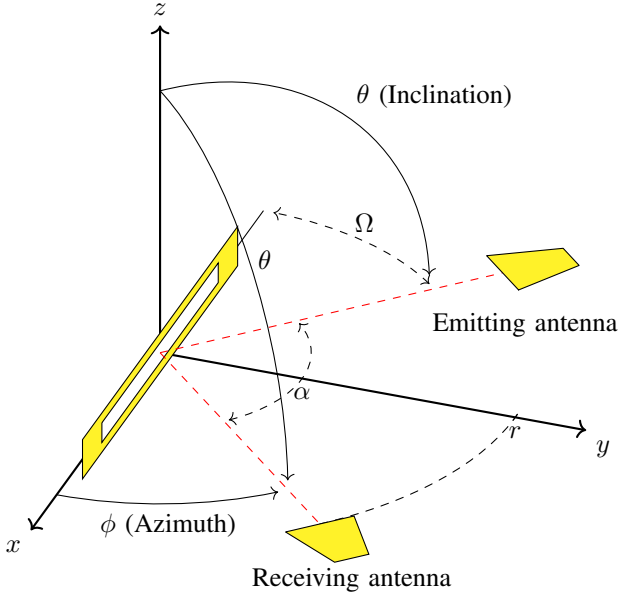


Fig. 1. Rectangular loop resonator made only of metal (without dielectric substrate), coordinate system and notations considered in this paper. The angle under study ϕ is between the resonator and the receiving antenna. Emitting and receiving antennas are positioned at the same angle θ both in monostatic ($\alpha = 0$) and bistatic ($\alpha \neq 0$) configurations.

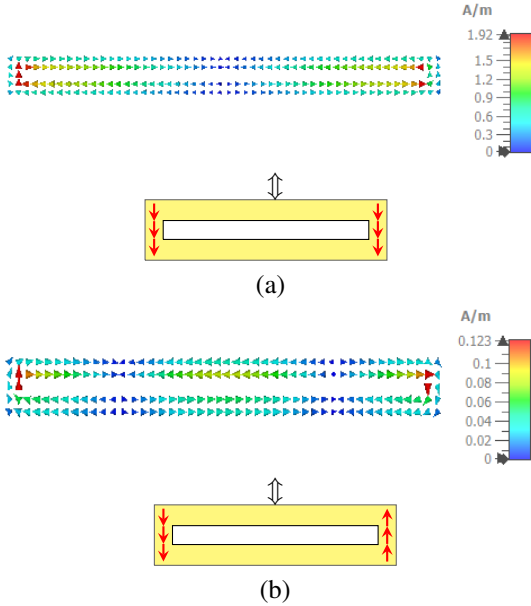


Fig. 2. Surface current obtained from simulation with a plane wave excitation at (a) the fundamental resonance frequency (even mode) and at (b) second resonance frequency (odd mode).



Fig. 3. Equivalent model of the loop resonator. The loop is replaced by two small dipoles spaced $\lambda/2$ apart with λ taken at the fundamental resonance frequency of the loop f_1 .

and the observation point of the E-field.

Hereafter, a subscript will indicate the integer n relative to

the resonance mode considered. At the fundamental frequency ($n = 1$), we have $kd = n \frac{2\pi}{\lambda} \cdot \frac{\lambda}{2} = \pi$ and $\beta = 0$. The total radiating field $E_s(f_1)$ amplitude (\vec{E}_s is along the z -axis) is :

$$\begin{aligned} E_s(f_1) &= E_d \times AF_1 \\ &= k_1 T_1 \sin(\theta) \frac{\sin(\pi \sin(\theta) \cos(\phi))}{\sin\left(\frac{\pi}{2} \sin(\theta) \cos(\phi)\right)} \end{aligned} \quad (2)$$

where

$$T_1 = \frac{\eta I_1 L}{16\pi r} \quad (3)$$

Using the same procedure, for the first harmonic ($n = 2$), we have $kd = n \cdot \frac{2\pi}{\lambda} \cdot \frac{\lambda}{2} = 2\pi$ and since it's an odd harmonic $\beta = \pi$ (see Fig. 2). The total radiated field amplitude $E_s(f_2)$ at the first harmonic can be written :

$$\begin{aligned} E_s(f_2) &= E_d \times AF_2 \\ &= k_2 T_2 \sin(\theta) \frac{\sin(2\pi \sin(\theta) \cos(\phi) + \pi)}{\sin(\pi \sin(\theta) \cos(\phi) + \frac{\pi}{2})} \\ &= 2k_2 T_2 \sin(\theta) \sin(\pi \sin(\theta) \cos(\phi)) \end{aligned} \quad (4)$$

where

$$T_2 = \frac{\eta I_2 L}{16\pi r} \quad (5)$$

The expressions of the total fields $|E_s(f_n)|$ are compared with the ones retrieved from a CST MW simulation in Fig. 4 and Fig. 5. In CST simulations, the loop is excited by an incoming plane wave with linear polarization (the wave propagates in the direction of the resonator and the electric field is along the z -axis) and the scattered E-fields have been normalized for the comparison. In Fig. 4, the simulated radiation pattern of the loop at the second harmonic in the plane $\phi = \pi/2$ is plotted and compared to the analytical model. In Fig. 5, the radiation pattern of the loop for different harmonics in the plane $\theta = \pi/2$ is plotted for both CST simulation and analytical model. We can see that the simulated radiation pattern of the loop and the one obtained with the introduced equivalent model are in good agreement. Note that contrary to the model, the full wave simulation used for the comparison takes into account all EM effect, such as coupling. However, since the results are almost identical, the analytical model can be used.

B. Expression of the current on the loop

We are now interested in the expression of the induced current on the loop in order to be able to compute T_1 and T_2 . The classical electrical equivalent model of a dipole in the receiving mode is shown Fig. 6.

The effective length of a dipole antenna is defined by [20] :

$$L_{\text{eff}} = V_{oc}/E_i \quad (6)$$

where V_{oc} is the open circuit voltage appearing across the antenna's terminal and E_i is the incident electric field on the antenna surface. Therefore, the current on the dipole I is :

$$I = \frac{V_{oc}}{Z_a + Z_l} = \frac{V_{oc}}{Z_a} = \frac{E_i \times L_{\text{eff}}}{Z_a} \quad (7)$$

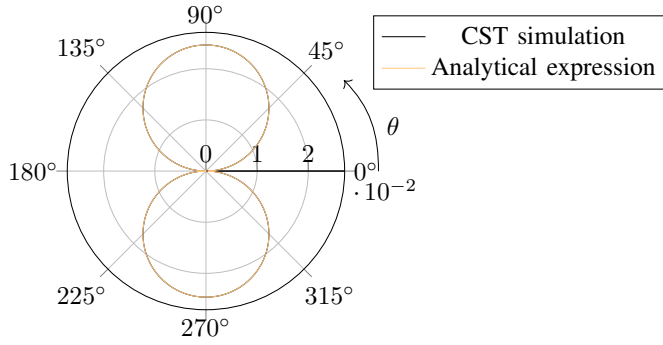


Fig. 4. Magnitude of the E-field (V/m) radiated by the loop with $\phi = \pi/2$ and $\theta \in [0^\circ; 360^\circ]$ at the second harmonic ($n = 3$). The wave propagates in the direction of the resonator and the electric field is along the z -axis.

where Z_a is the antenna impedance and Z_l the load impedance which is considered to be equal to zero as the dipole is in short circuit. It should be noted that the effective length is also a far-field quantity and it is related to the far-zone field E_a radiated by the antenna, with current I in its terminals, by :

$$E_a = -j\eta \frac{kI}{4\pi r} L_{\text{eff}} e^{-jkr} \quad (8)$$

After identification with (2) and (8) considering the same current on the dipole and the same frequency, we have :

$$L_{\text{eff-n}} = \frac{L}{2} \sin(\theta) \times AF_n \quad (9)$$

Thereafter, the ratio T_2/T_1 can be expressed using (7) and (9) as :

$$\frac{T_2}{T_1} = \frac{I_2}{I_1} = \frac{L_{\text{eff-2}} \times Z_a(f_1)}{L_{\text{eff-1}} \times Z_a(f_2)} = \frac{Z_a(f_1) AF_2(\Omega)}{Z_a(f_2) AF_1(\Omega)} \quad (10)$$

Since we are consider the received power, the angle that needs to be used in the array factor is Ω , i.e. the angle between the resonator and the emitting antenna. The value of Ω can be calculated using Fig. 1 and is equal to :

$$\Omega = \pi - \alpha - \phi \quad (11)$$

Concerning the expression of the impedance Z_a of the antenna to be considered, without any assumption, it corresponds to the infinitesimal dipole modelled until now. Indeed, the surface currents induced at the top and bottom arms of the loop are in phase opposition and does not contribute to the radiation. The latter is obtained by considering, as before, that the radiation of the antenna is linked to the vertical part of the loop modeled by an infinitesimal dipole and its expression is given by [20, p. 179] :

$$R_a = 80\pi^2 \left(\frac{L}{\lambda} \right)^2 \quad (12)$$

Thus, the coefficient $\frac{Z_a(f_1)}{Z_a(f_2)}$ is a constant that is equal to :

$$\frac{Z_a(f_1)}{Z_a(f_2)} = \left(\frac{\lambda_2}{\lambda_1} \right)^2 = \frac{1}{4} \quad (13)$$

Equation (10) can be compared to full-wave simulation results. Using CST MW, the maximum value of the electric-field

is measured under different incidence angles Ω of the emitting antenna with the loop resonator with the same dimensions as the ones given in the legend of Fig. 7. The results are plotted in Fig. 8. We can observe that the model and the simulation are in good agreement which validates the model.

C. Azimuthal angle determination

From (2), (4), (10) and (13), it is possible to measure the azimuthal angle ϕ , i.e. the rotation of the loop resonator around the z -axis (ϕ) as shown in Fig. 1. By dividing (2) and (4), we have :

$$\frac{E_s(f_2)}{E_s(f_1)} = 2 \frac{k_2 T_2(\Omega)}{k_1 T_1(\Omega)} \sin\left(\frac{\pi}{2} \sin(\theta) \cos(\phi)\right) \quad (14)$$

Finally, by replacing (10) and (13) :

$$\begin{aligned} \frac{E_s(f_2)}{E_s(f_1)} &= 4 \frac{k_2 Z_a(f_1)}{k_1 Z_a(f_2)} \sin\left(\frac{\pi}{2} \sin(\theta) \cos(\phi)\right) \\ &\times \sin\left(\frac{\pi}{2} \sin(\theta) \cos(\Omega)\right) \\ &= 2 \sin\left(\frac{\pi}{2} \sin(\theta) \cos(\phi)\right) \\ &\times \sin\left(\frac{\pi}{2} \sin(\theta) \cos(\pi - \alpha - \phi)\right) \end{aligned} \quad (15)$$

Equation (15) is particularly interesting as it is independent of the geometric quantities describing the resonator or the distance r between the scatterer and the antennas. It is thus possible to use this equation to derive the angles without any calibration step or knowledge on the distance r , which is very different from the angle measurement approaches already introduced in chipless RFID. By calibration step, it means a first measurement of the tag at a known distance and a known angle in order to apply the approach. Here such a measurement is not needed to use (15) to determine the Azimuthal angle. Note that a calibration is a post-processing step very different from a measurement of the environment without the tag (noted hereafter empty measurement) to perform a background subtraction. Indeed, the measurement of the empty environment allows to isolate the signature of the tag from its environment what is very appreciable in RFID chipless. It is a very often essential stage commonly used and which will be also implemented in the part measurement of the article. However, this empty measurement is done without the tag, which is very different from a calibration measurement which needs to be done for a perfectly known configuration of the tag. With this additional measurement, it is generally possible to implement more specific and therefore often restricted approaches in terms of use or to improve the resolution. One of the advantages of the theoretical development introduced here is to be able to free oneself from this type of additional measurement which are often much more constraining to implement in practice compared to an empty measurement which can be done automatically when no tag is present in the reading zone.

In practice, by using a VNA, we will only be able to measure S-parameters. With the radar equation, the incoming power P_y on the port y of the VNA and the emitted power

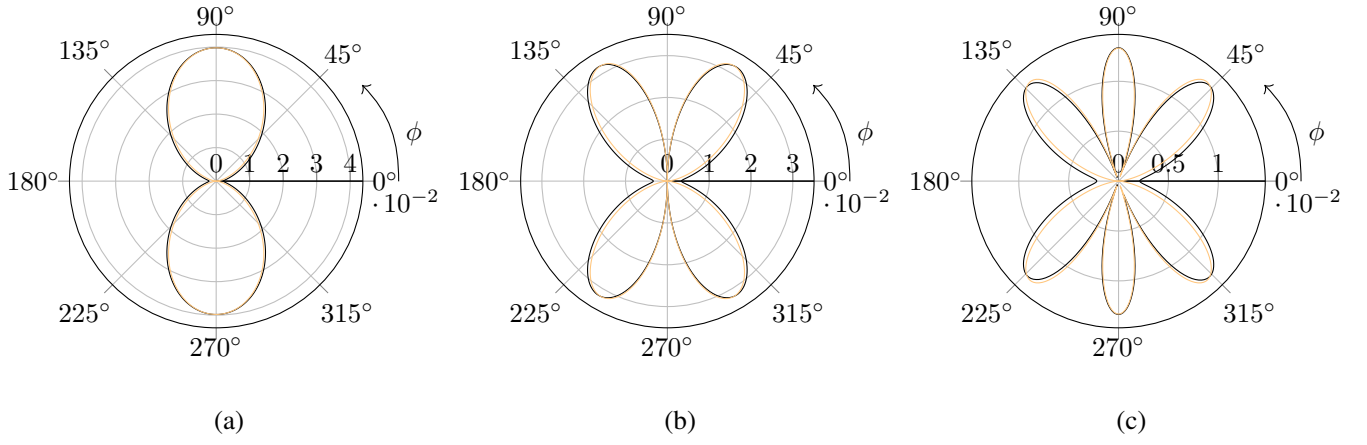


Fig. 5. Magnitude of the E-field (V/m) radiated by the loop with $\theta = \pi/2$ and $\phi \in [0^\circ; 360^\circ]$ at (a) the fundamental frequency, (b) the first harmonic and (c) the second harmonic. In black the CST simulation and in yellow the expressions obtained from the loop model. The wave propagates in the direction of the resonator and the electric field is along the z -axis.

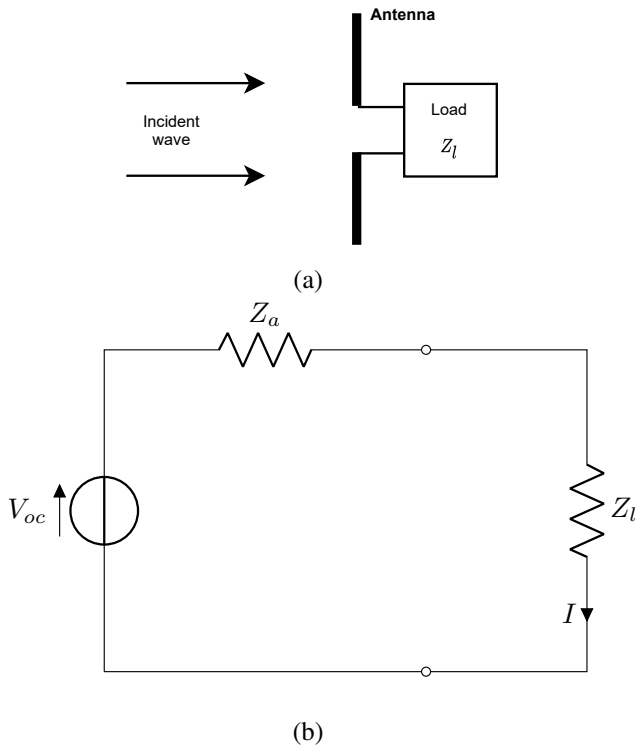


Fig. 6. (a) Antenna in the receiving mode and (b) its electrical equivalent model where Z_a is the antenna impedance, Z_l the load impedance and V_{oc} the open circuit voltage appearing across the antenna's terminals.

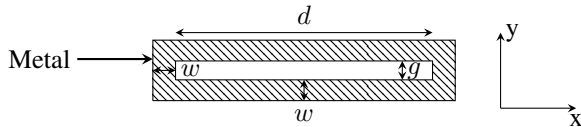


Fig. 7. Loop resonator used for the orientation extraction. Dimensions : $d = 47.97$ mm, $g = 2.07$ mm and $w = 1.43$ mm. Metal is $100 \mu\text{m}$ thick. The resonance frequency for this dimension is 3GHz.

P_x on the port x and the definition of S-parameters, we have:

$$|S_{xy}|^2 = \left| \frac{P_y}{P_x} \right| = \frac{G_t(\theta, \phi) G_t(\theta, \Omega) G G' \lambda^4}{(4\pi)^4 R_0^2 R_1^2} \times (1 - |\Gamma|^2) \times (1 - |\Gamma'|^2) \quad (16)$$

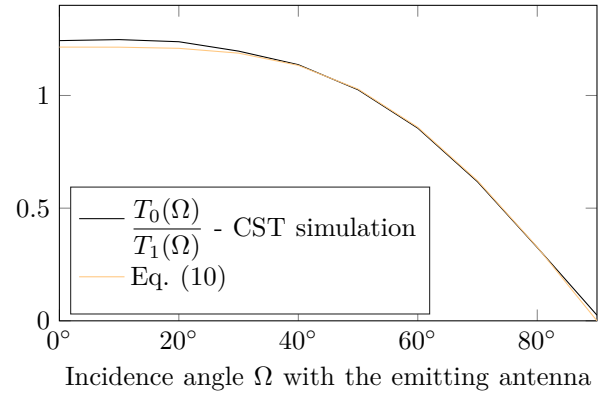


Fig. 8. Comparison between $T_1(\Omega)/T_2(\Omega)$ extracted from CST simulation and (10).

where G and G' are the gain of the emitting and receiving antennas respectively, R_0 and R_1 the distances between the emitting and receiving antennas with the resonator, Γ and Γ' the reflection coefficients respectively for emitting and receiving antenna. S_{xy} can correspond to a mono-static configuration with S_{11} or S_{22} or to a bi-static configuration with S_{21} or S_{12} . G_t is the gain of the resonator. In case of the loop resonator with the model previously presented, it is possible to analytically calculate its gain with [20, p. 155] :

$$G_t = 4\pi \frac{\frac{r^2}{2\eta} |E|^2}{\int_0^{2\pi} \int_0^\pi \frac{r^2}{2\eta} |E|^2 \sin(\theta) d\theta d\phi} \quad (17)$$

where η is the intrinsic impedance of the medium and the radiated E-field E can be computed using (2) or (4) for example. We have :

$$G_t(\theta, \phi, f_i) = a(i) \times \sin(\theta)^2 \times A F_i(\theta, \phi)^2 \quad (18)$$

where we can calculate for the first two resonances using (17) :

$$a(i) \simeq \begin{cases} \frac{4\pi}{14.20}, & \text{for } i = 0 \\ \frac{4\pi}{16.47}, & \text{for } i = 1 \end{cases} \quad (19a)$$

$$(19b)$$

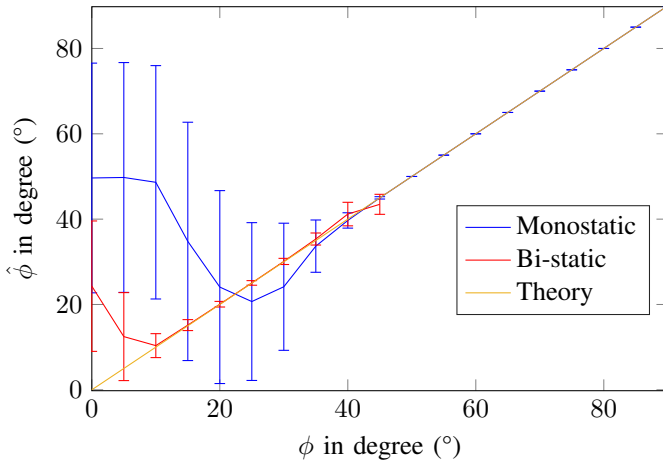


Fig. 9. Monte-Carlo simulation : the uncertainty of the extracted angle $\hat{\phi}$ as a function of the real angle ϕ is plotted for both configurations. The bi-static configuration uses a value of $\alpha = 45^\circ$. Vertical bars represent the standard derivation on $\hat{\phi}$. The considered SNR is 40dB.

By dividing (16) for the first two harmonics (f_1 and f_2), we obtain (20) which is (15) in terms of S-parameters.

$$\begin{aligned} \left| \frac{S_{xy}(f_2)}{S_{xy}(f_1)} \right| &= 0.86 \times \sqrt{\frac{G(f_2)G'(f_2)}{G(f_1)G'(f_1)}} \\ &\times \sqrt{\frac{1 - |\Gamma(f_2)|^2}{1 - |\Gamma(f_1)|^2}} \times \sqrt{\frac{1 - |\Gamma'(f_2)|^2}{1 - |\Gamma'(f_1)|^2}} \\ &\times \sin\left(\frac{\pi}{2} \sin(\theta) \cos(\phi)\right) \\ &\times \sin\left(\frac{\pi}{2} \sin(\theta) \cos(\pi - \alpha - \phi)\right) \end{aligned} \quad (20)$$

In our case, QH2000 antennas are used in practice with the antenna gain and matching Γ provided by the manufacturer [21]. So, (20) and (15) can be translated into S-parameters to :

$$\begin{aligned} \left| \frac{S_{xy}(f_2)}{S_{xy}(f_1)} \right| &= 2.42 \sin\left(\frac{\pi}{2} \sin(\theta) \cos(\phi)\right) \\ &\times \sin\left(\frac{\pi}{2} \sin(\theta) \cos(\pi - \alpha - \phi)\right) \end{aligned} \quad (21)$$

D. Uncertainty

A Monte-Carlo simulation was done in order to estimate the robustness of the proposed method. Both mono-static and bi-static configurations have been studied. Simulation results are plotted in Fig. 9. The true angle ϕ varies from 0° to 90° and the estimated angle $\hat{\phi}$ is extracted with an SNR of 40 dB which corresponds to the classical noise observed in measurement.

To achieve such results, first CST simulations have been realized for different angle values (from 0° to 90° as shown in Table II). The corresponding S-parameters have been then exported to Matlab. A white gaussian noise with a standard deviation corresponding to a SNR of 40 dB has been added to both real and imaginary parts of the 10.000 S-parameter points. Then (23) or (26b) has been applied to the S-parameters with noise and the uncertainty information have been extracted from the obtained estimated angles using Matlab dedicated functions.

When measurements are corrupted by noise, this noise impacts the estimators by two different ways: a bias, which is a systematic error between the estimated value and the true orientation of the tag (characterized by the mean of the estimator); and a random error, which can be characterized by its standard deviation (uncertainties). With this method, both the errors and the uncertainties are presented in the manuscript. We can notice that for low ϕ angle values, the mono-static approach has high uncertainties below 40° and can not be used for ϕ angles below 15° with an error lower than $< 7^\circ$ (these data have been reported in Table I for clarity). Indeed, the instantaneous estimation in mono-static for a value of ϕ between 15° and 40° can have an uncertainties of 15° but, on average, the error is very low beyond an angle of 15° . Note that common VNAs natively implement average functionalities allowing to use this approach as low as 15° for the mono-static case for this given SNR. Hence, using an averaging technique to lower the uncertainties impacts, the sensing can go as low as 15° for the mono-static given its error bias. For the bi-static configuration, this angle can go as low as 5° as shown in Fig. 9.

Hence the bi-static is more robust than the mono-static configuration. These remarks will be further illustrated in the measurement part. In the Monte-Carlo simulation (see Fig. 9), the residual environment is modeled by additive gaussian noise and considering that the variance is a function of the distance.

Simulation presented in Fig. 9 can be used to maximize the correctness of the sensor in bi-static configuration where an optimal setup can be obtained when $\alpha = 54^\circ$. Indeed, it is possible to vary α in the Monte-Carlo simulations in order to obtain the largest measuring range for the sensor (largest range with an error lower than 7°).

Mono-static and bi-static approaches have been studied because they both bring their own advantages and disadvantages and the model described previously can be used to characterize the performance of both approaches. The cost of a mono-static measurement is lower since only one antenna is required compared to a bi-static approach. Additionally, a mono-static measurement gives one solution of ϕ while the bi-static gives two solutions due to the periodicity of (15) as a function of α . Furthermore, the bi-static introduces errors in practice because the angle α need to be determined while this parameter does not exist for the mono-static configuration. Besides these disadvantages, the bi-static offers advantages like a higher precision on the extracted angle, a lower uncertainty and the possibility to sense very low angles. Last but not least, a setup with two antennas can be used to take advantage of both configurations. Starting by measuring S_{11} (mono-static approach) only one solution will be found. After that, a S_{21} measurement (bi-static approach) can be done to extract the angle with a higher precision and lower uncertainty. Two solutions will be found with the periodicity of (15) but the correct one can be found since it will be the closest to the one measured with S_{11} . A comparison between both mono-static and bi-static antenna configurations is provided in Table I.

TABLE I

COMPARISON OF MONO-STATIC AND BI-STATIC CONFIGURATIONS

	Mono-static	Bi-static
Cost	Lower cost (1 antenna)	Higher cost (2 antennas)
Uncertainties	Higher	Lower
Precision	Lower	Higher
Theoretical number of solution ($\phi \in [0^\circ-90^\circ]$)	1	2
Theoretical lowest measurable angle with SNR 20dB and $< 7^\circ$ error	15°	5°

TABLE II

SIMULATION (CST) IN MONO-STATIC ($\alpha = 0^\circ$)

ϕ	0°	10°	20°	30°	40°	50°	60°	70°	80°	90°
$\hat{\phi}$	28°	26°	21°	27°	40°	51°	61°	70°	80°	88°

TABLE III

SIMULATION (CST) IN BI-STATIC ($\alpha = 90^\circ$)

ϕ	0°	10°	20°	30°	40°	50°	60°	70°	80°	90°
$\hat{\phi}$	0°	11°	20°	30°	40°	50°	56°	70°	80°	90°

III. SIMULATIONS

Simulations have been carried out using CST MW to validate the introduced approach to estimate the orientation ϕ of a loop. The transient solver with a plane wave excitation was used. So the azimuthal angle ϕ is extracted using (15), and the backscattered E-field E_s is obtained using far-fields probes in the simulator. The loop dimensions also used in the measurement part are given in Fig. 7. Results are given in Table II and Table III. We see that the estimated angle $\hat{\phi}$ is in good agreement with the simulated angle ϕ . Both mono and bi-static antenna configurations were simulated and validated, thus allowing the possibility to use the desired one as a final application. A noticeable point is the obtained measurable range : in bi-static the estimated angle is accurate down to 0° , but for the mono-static configuration the estimated angle cannot go lower than 30° limiting the measurable range to $[30^\circ; 90^\circ]$. The reason behind this limitation has been discussed in section II-D and is illustrated in Fig. 10. In the mono-static case, when the incidence angle ϕ is small, antenna aperture of the loop is small both for the wave reaching the loop and for the wave backscattered to the antenna. This case is different in bi-static, where it is clear that the receiving antenna is positioned in a favorable direction, namely at the main lobe of the loop antenna. It is for this reason that in a mono-static configuration below 30° , the estimated angle is constant because the backscattered E-field is equal to the noise floor.

For this reason, to improve the measurable range and precision, we can use a bi-static configuration or even higher harmonics. Indeed, by looking at the radiation pattern of the second harmonic in Fig. 5c, we can see that we have a maximum of power around 45° thus allowing a higher back-

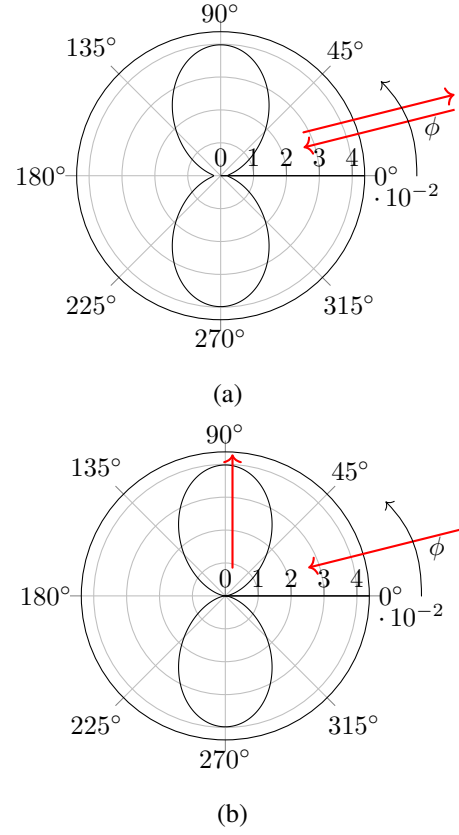


Fig. 10. (a) Path followed by the electromagnetic wave when the incidence ϕ is small in a mono-static case and (b) in a bi-static case.

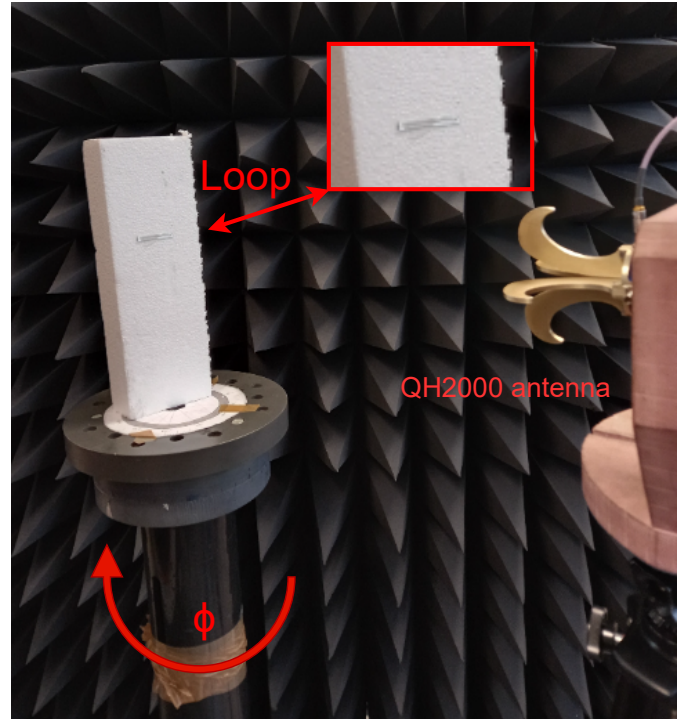


Fig. 11. Setup used for the extraction of ϕ - mono-static configuration ($\alpha = 0^\circ$).

scattering power for small values of ϕ . Indeed, this second

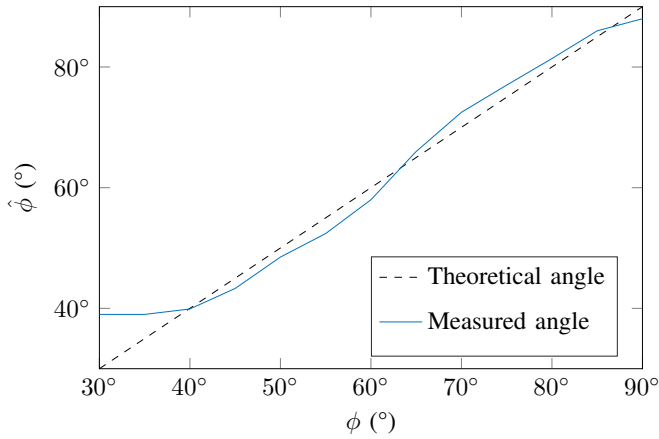


Fig. 12. Measurement in mono-static configuration ($\alpha = 0^\circ$). The estimated angle $\hat{\phi}$ is plotted as a function of the real angle ϕ .

harmonic $E_s(f_2)$ for example, can be used instead of the first harmonic in (15) with the following equation to extend the measuring range :

$$\frac{E_s(f_3)}{E_s(f_1)} = \frac{1}{3} (2 \cos(\pi \cos(\phi)) - 1) \times (2 \cos(\pi \cos(\Omega)) - 1) \quad (22)$$

Notice that the higher uncertainty and error of the mono-static approach are predicted by the Monte-Carlo simulation (see Fig. 9).

IV. MEASUREMENTS

Now that the extraction of the loop orientation is validated in simulation, real measurements are considered both in mono and bi-static configuration. Measurements for the mono-static configuration were done following the test bench shown in Fig. 11. For the bi-static configuration, the same setup is used but with a second antenna placed at $\alpha = 90^\circ$ from the first one. The tag is placed on top of a rotating pillar (about 15 cm away using a piece of foam to isolate the loop from the pillar which is very reflective). The protocol used for the measurement is the following : the S-parameters are measured using the VNA (Keysight P9375A) for the tag being rotated from 5° to 90° in relation to the antenna with a 5° step (the antenna is perpendicular to the loop for $\phi = 90^\circ$ as described in Fig. 1). If we place the antenna at $\theta = 90^\circ$, (21) can be simplified to:

$$\left| \frac{S_{xy}(f_2)}{S_{xy}(f_1)} \right| = 2.42 \sin\left(\frac{\pi}{2} \cos(\phi)\right) \times \sin\left(\frac{\pi}{2} \cos(\pi - \alpha - \phi)\right) \quad (23)$$

For each angle, (23) is used to determine $\hat{\phi}$. A first measurement without the resonator is subtracted to the other measurements (with the resonator) to remove the response of the environment [22]–[24]. Raw measurements directly measured with the VNA are used without any post-processing.

A. Mono-static configuration

The mono-static configuration offers several advantages, such as the fact that it is easier to implement as presented

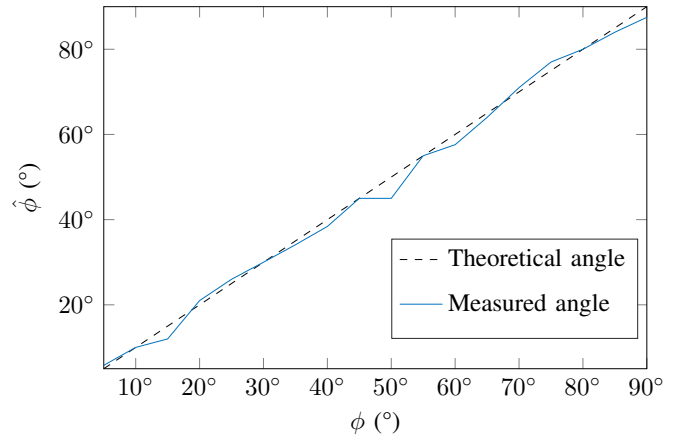


Fig. 13. Measurement in bi-static configuration with $\alpha = 90^\circ$. The estimated angle $\hat{\phi}$ is plotted as a function of the real angle ϕ .

in Table I. For these reasons, the mono-static configuration (case $\alpha = 0^\circ$) is first considered. Measurements were done following the test bench described in Fig. 11 and the results are given in Fig. 12. The resonator is 20 cm away from the antenna.

The obtained results are in good agreement with those previously described in the simulation (Section II.D) : the mono-static configuration can be used with a very good accuracy for angles higher than 40° . Indeed, in the simulation, the limit angle was equal to 30° , in practice due to a higher noise floor, this angle is near 40° . Overall, the estimated angle is in good agreement with the real angle validating the potential of this approach. In the range 40° - 90° , the maximum error measured is 2.6° when the real angle is equal to 55° . Below a real angle of 40° , measured errors are getting higher with almost 10° for a real angle of $\phi = 30^\circ$ as predicted by Monte Carlo simulations. Below 30° , errors were too high to extract any angle.

B. Bi-static configuration

Fig. 13 presents the estimated angle $\hat{\phi}$ alongside the real angle ϕ . We can see that the extracted angle $\hat{\phi}$ is in good agreement with the real value ϕ . The highest error is obtained at 50° with a difference of 5° . As the Monte-Carlo showed, the measured quantities are in very good agreement with the real angle with value as low as $\phi = 10^\circ$.

V. GENERALISATION OF THE APPROACH

In sections III and IV, we have considered $\theta = 90^\circ$ but the proposed model is more general and allows the estimation of both the inclination θ and the azimuthal ϕ angles. If we consider a configuration with two antennas where both antennas have the same inclination θ (as illustrated in Fig. 1), with (21), we can have by measuring S_{11} :

$$\frac{S_{11}(f_2)}{S_{11}(f_1)} = 2.42 \sin\left(\frac{\pi}{2} \sin(\theta) \cos(\phi)\right)^2 \quad (24)$$

By using the S_{22} parameter, we can also have :

$$\frac{S_{22}(f_2)}{S_{22}(f_1)} = 2.42 \sin\left(\frac{\pi}{2} \sin(\pi - \alpha - \theta) \cos(\phi)\right)^2 \quad (25)$$

TABLE IV

ESTIMATED ANGLES ($^\circ$) OF THE EMITTING ANTENNA USING (26A) IN SIMULATION FOR (A) θ AND (B) ϕ IN SIMULATION.

$\theta \backslash \phi$	80	70	60	$\theta \backslash \phi$	80	70	60
90	90	90	90	90	80	70	60
80	79	79	80	80	80	70	60
70	69	71	68	70	80	68	59
60	59	57	56	60	79	68	57
50	52	45	53	50	79	66	52

(a)
(b)

Thus, by solving the system of equations composed of (24) and (25), the following equations can be obtained :

$$\phi = \arccos \left(\frac{1}{\sin(\theta)} \frac{2}{\pi} \arcsin \left(\sqrt{\frac{S_{11}(f_2)}{2.42S_{11}(f_1)}}} \right) \right) \quad (26a)$$

$$\theta = \cot^{-1} \left(\csc(\alpha) \left[\frac{\arcsin \left(\sqrt{\frac{S_{22}(f_2)}{2.42S_{22}(f_1)}}} \right)}{\arcsin \left(\sqrt{\frac{S_{11}(f_2)}{2.42S_{11}(f_1)}}} \right)} - \cos(\alpha) \right] \right) \quad (26b)$$

Note that (26b) can be used to estimate θ . After that, $\hat{\theta}$ can be injected in (26a) to estimate ϕ . Note also that S_{21} parameter means signal coming from antenna 2 to antenna 1 but both antennas share the same polarization axis (along the resonator arms).

A. Simulations

Simulations have been done in order to validate this approach. The simulated configuration is the same as in Section III but now, both θ and ϕ can change simultaneously and (26a) is applied on the simulated results. Results are plotted in Table IV. We can see that extracted quantities are in good agreement with the expected ones. Errors increase as angles values decreases (as stated before in Section II) with a maximum error of 8° on $\hat{\phi}$ at $\phi = 60^\circ$ and $\theta = 50^\circ$.

B. Measurements

A semi anechoic environment (MVG StarLab) has been used to validate the excitation of both θ and ϕ in measurement. The setup is illustrated in Fig. 14. The loop resonator is horizontally placed on top of the central pillar. The pillar can rotate along its axis resulting a variation of the angle ϕ between the loop and the antennas. Also, the orange arch can rotate resulting in a variation of the angle θ of the tag with the antennas. Due to the StarLab configuration, the measuring range is limited to $60^\circ < \phi < 80^\circ$ with a step of 10° and $60^\circ < \theta < 70^\circ$ with a step of 3° . An averaging on 36 samples on the VNA is used to lower the noise floor. The resonator is placed 45 cm away from the antenna. The angle α is equal to 30° . Equation (26a) is used and results are plotted in Table V. The angle $\hat{\phi}$ is well estimated with a maximum error of 4° for $\phi = 60^\circ$ and 1.5° on average. The angle $\hat{\theta}$ is estimated with higher errors and a maximum error of 9° (2.8° on average). An example of measured S-parameters is presented in Fig. 15.

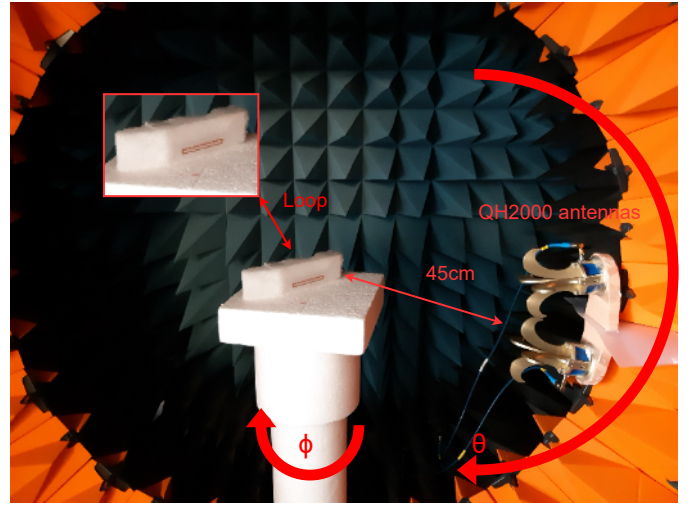


Fig. 14. Measurement setup in semi anechoic environment to determine the orientation of the antenna (extraction of θ and ϕ). The angle $\alpha = 30^\circ$.

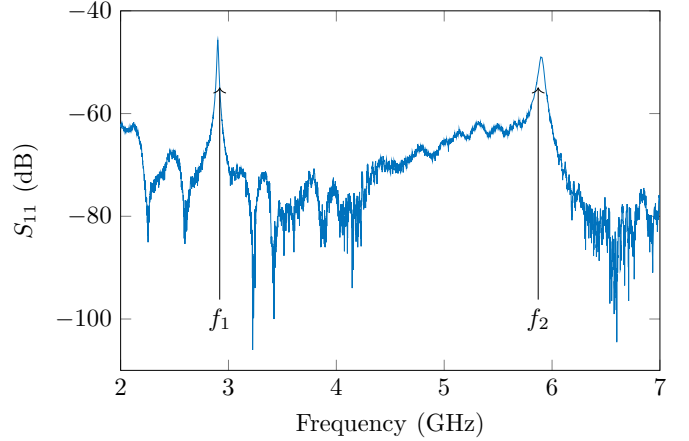


Fig. 15. Measured S-parameters where the empty measurement have been subtracted for a value of $\phi = 70^\circ$ and $\theta = 84^\circ$ in the Starlab for a distance resonator-antenna of 45 cm.

TABLE V

ESTIMATED ANGLES ($^\circ$) OF THE EMITTING ANTENNA USING (26A) IN PRACTICE FOR (A) θ AND (B) ϕ IN PRACTICE.

$\theta \backslash \phi$	80	70	60	$\theta \backslash \phi$	80	70	60
60	57	62	56	60	78	68	56
63	63	52	52	63	79	69	58
66	64	66	64	66	78	69	59
70	74	79	69	70	78	68	56

(a)
(b)

C. Monte-Carlo simulations

Monte Carlo simulations have been done on (26a) and (26b) in order to estimate errors and uncertainties on the extracted quantities $\hat{\phi}$ and $\hat{\theta}$ and results are plotted in Fig. 16 and Fig. 17 for $\hat{\phi}$ and $\hat{\theta}$ respectively. We can see that for $\hat{\phi}$, errors and uncertainties are quite low except when $\theta > 60^\circ$ and $\phi < 20^\circ$. Elsewhere, the errors are below 1° and uncertainties are below

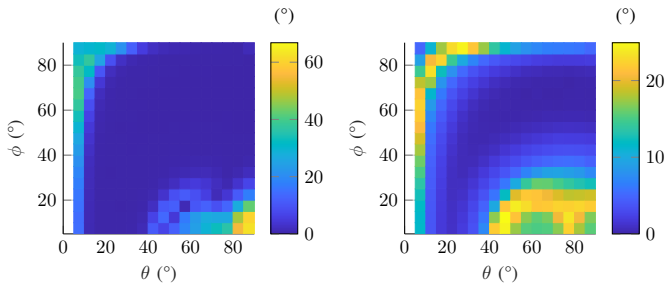


Fig. 16. (a) Errors and (b) uncertainties on the estimated angle $\hat{\theta}$ as a function of real values of (θ, ϕ) with a SNR of 40dB.

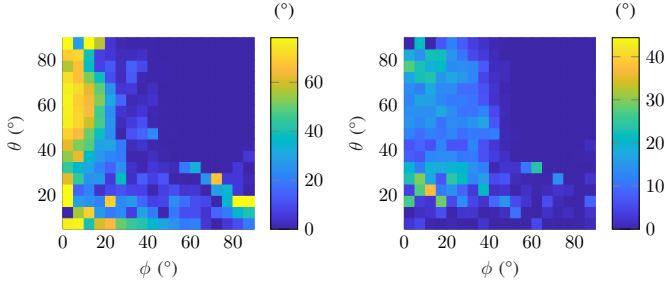


Fig. 17. (a) Errors and (b) uncertainties on the estimated angle $\hat{\phi}$ as a function of real values of (θ, ϕ) with a SNR of 40dB.

1° when $\phi > 40^\circ$ but increase up to 15° for $20^\circ < \phi < 40^\circ$. For $\hat{\theta}$ errors are lower than 1° except when we are close to $\phi = 90^\circ$ or $\theta = 90^\circ$. In practice, due to the StarLab limitations, measurements were done in the range of $60^\circ < \phi < 80^\circ$ and $60^\circ < \theta < 70^\circ$ which, according to the Monte-Carlo simulation results, corresponds to a favorable configuration.

VI. REAL ENVIRONMENT MEASUREMENT

In this section, we want to show potential applications of the proposed approach. These applications have in common that they are implemented in a real environment, namely in an office-type room. In the first part, we will focus on the accuracy of measurement obtained in this type of environment. We will be particularly attentive to the undesirable effects linked to the presence of objects near the tag. These effects will be quantified by characterizing the limitation induced on the reading distance as well as the angular range of the sensor. The second part will present application examples in a more constrained environment (resonator placed on a plastic card moved by hand in front of the reader). We will see that despite the presence of these objects near the tag, it is possible to use the proposed solution to track in real time the movements of the card. Indeed, we will see that for this type of application, it is not necessary to have a very good precision in the extraction of the angles but rather to be able to extract the information from a method that is very inexpensive in terms of calculation time. The measurement protocol in these section is the same as in section IV. Table VI summarizes the information of the different setup used in this section.

A. Limitation in real-life environments

Previous measurements were done in semi-anechoic environment. This section is dedicated to real environment

TABLE VI
DIFFERENT SETUP CONFIGURATION USED IN SECTION VI.

Measurement section	VI.A.a	VI.A.b	VI.B
Setup illustration	Fig. 18	Fig. 22	Fig. 25
Distance antenna-loop	Variable	20 cm	<10 cm
Antenna configuration	monostatic	monostatic	Mono and bi-static
Antenna model	QH2000 & QH800	QH2000	QH2000
Frequency band	2-7GHz	2-7GHz	2-7GHz
Number of points	2001	2001	100
IF bandwidth	10kHz	10kHz	10kHz
Time-gating	No	No	No
Averaging	No	No	No
Empty measurement	Yes	Yes	Yes
Loop geometry	Fig. 7	Fig. 7	Fig. 7
Support	Polystyrene	Plastic box	Credit card

measurements. The measurement setup of Section IV-A (mono-static configuration) is repeated in an office (approximately $8m^2$) without any anechoic walls and for different distances resonator-antenna. The test bench is illustrated in Fig. 18; an example of measured S-parameters is presented in Fig. 19. The extracted ϕ angles are given in Fig. 20 where in plain line, the angle estimation in the office is done for different distances. The angle estimation done in Section IV with a semi anechoic environment is also presented (dashed red) for comparison. We can see that in a real environment, the lower bond of the measuring range angle increases as the distance resonator-antenna increases. This can be explained using the Monte-Carlo simulation (see Fig. 9) and the link between distance and SNR [25]. Indeed, the minimum measurable backscattered signal amplitude can be seen in Fig. 19. The measured resonant frequency peak apex can not be lower than $-60dB$ and as shown in (16) the signal levels are a function of the distance between the tag and the antenna. Thus, it is possible to relate Fig. 19 to a Monte Carlo study (Fig. 21) where the error has been calculated for different SNR values. Comparing the two figures, it is very clear that increasing the reading range reduces the SNR and therefore increases the measurement error and more significantly reduces the range of use of the sensor by limiting the angles for which measurement is possible. We can notice in Fig. 21, that errors start to appears for $\phi = 90^\circ$ (first harmonic should be zero) when the SNR decreases but also the lower bond of the measuring range increases (when the fundamental and the first harmonic come close to zero) which was confirmed in practice in Fig. 20. We can also see in Fig. 20 (black line) that by using an antenna with a higher directivity (QH800 [21]), the measuring range is increased by 30 cm. Indeed, the higher is the gain, the lower is the residual environment [25] but also the backscattered signal from the loop is higher meaning a higher SNR. Note that the Monte-Carlo simulations are a good way to predict the measurable range in practice for a given environment knowing its SNR. Moreover, the introduced formulas are not sensitive to the distance variation between the tag and the antennas nor to the geometry of the loop. Indeed, the formulas can be applied without any indication on the distance between the resonator and the antennas. However, in practice, the SNR is

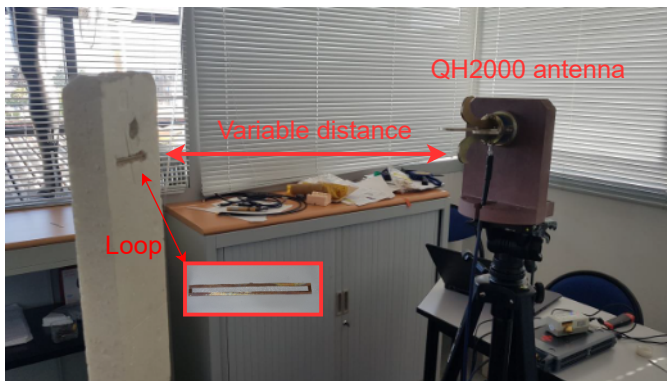


Fig. 18. Test bench configuration for the mono-static measurement in an office.

a function of the distance, which will limit it. This is why the measurement distances are those classically found in chipless applications. The measurement noise is also linked to the environment, typically to the presence and the variation over time of objects placed near the tag. In practice, we observe a measurement distance of around 50 cm in a controlled real environment (no or few objects near the tag), this distance can be reduced to 20 cm if the environment near the tag changes during the measurement. Monte-Carlo simulations can be performed to estimate the measuring range knowing the SNR of the environment.

Measurements through a lossy object have also been carried out. A plastic box was used as a container as showed in Fig. 22. The distance between the resonator and the antenna is 20 cm. The resonator was either placed inside the box or on its side and estimations are presented in Fig. 23. We can see that the response is similar to the previous case without any obstacle between the resonator and the tag (see Fig. 20). So the plastic had a limited impact of the estimation. The sensor functionality seems more viable when the resonator is placed on the side of an obstacle if an obstacle is present. Again by using an antenna with a higher gain, the measuring range is improved as illustrated in Fig. 24.

B. Real time angular tracking application

Two examples of real-time applications in real-life are presented below as a proof of concept of this approach. To see concretely the achievable performances for a real time application, two videos have been made [26], [27]. In these videos, the loop angular sensor is used to allow a user to interact with an electronic equipment (the chipless reader). The loop is fixed on a plastic card in credit card format. The reader is composed of one or two antennas (depending on the reading mode recommended, i.e. extraction of information on one [26] or two angles [27]), a VNA for the measurement of the S parameters and a computer that performs the calculations and controls the VNA. The real time information of the angular position of the card is displayed on the PC screen. A user holds in his hand the plastic card. When he puts the card above the antenna (see Fig. 25) the reader detects the angle of the loop and displays it in real time on a computer screen (using

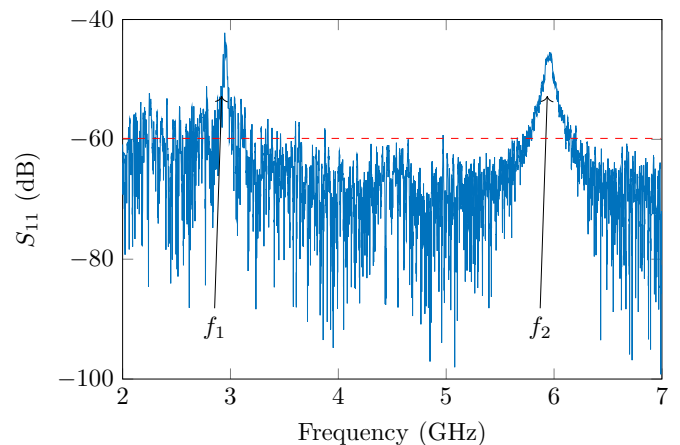


Fig. 19. Measured S-parameters with the empty measurement for a value of $\phi = 70^\circ$ and $\theta = 90^\circ$ in the office for a distance resonator-antenna of 20 cm. An averaging of 5 samples is used.

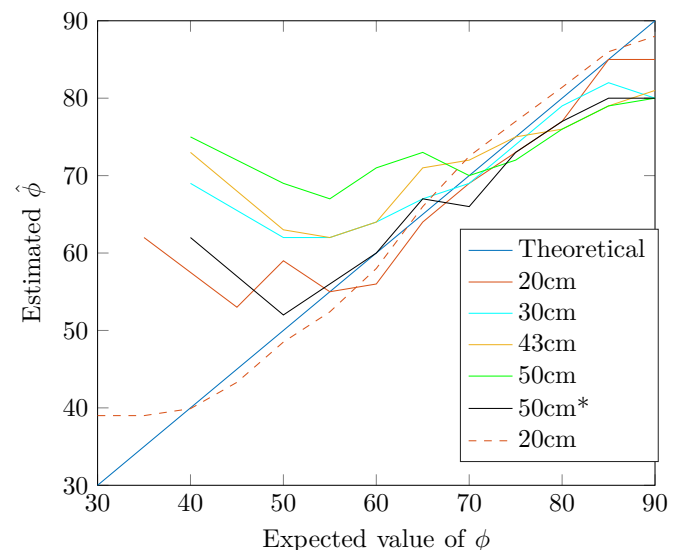


Fig. 20. Estimated value of ϕ in an office for different distances between the tag-antenna. In dashed line, the measurements done in Section IV in semi-anechoic environment. The estimation in black annotated by "*" is done with a different antenna (higher gain - QH800 [21]).

Matlab). Note that in these two examples, measurements are done in a real environment with the presence of humans nearby as well as scattering objects (human hand, plastic card). No alignment (such as calibration measurements) between the antenna and the resonator is performed, the user just place its card above the antenna.

The video [26] presents the mono-static configuration (see Fig. 25a), where only the azimuth angle is detected (see (23)). In the video [26], on the left is shown the hand holding the resonator in front of the antenna (QH800). On the right is presented the real time estimated azimuth angle on a Matlab figure. The fixed green arrows represent the coordinates system. The black line corresponds to the loop resonator. The red arrow is orthogonal to the loop resonator showing the direction in which the resonator aims. In this experiment, several distances between the tag and the antenna

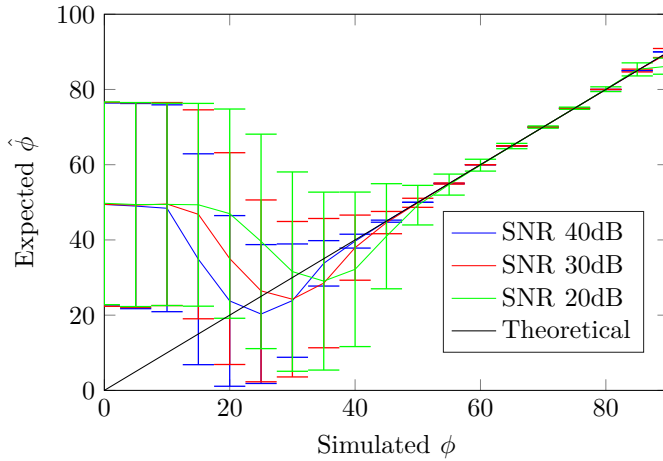


Fig. 21. Monte Carlo simulations for different values of SNR for a mono-static configuration as a function of ϕ while $\theta = \pi/2$.

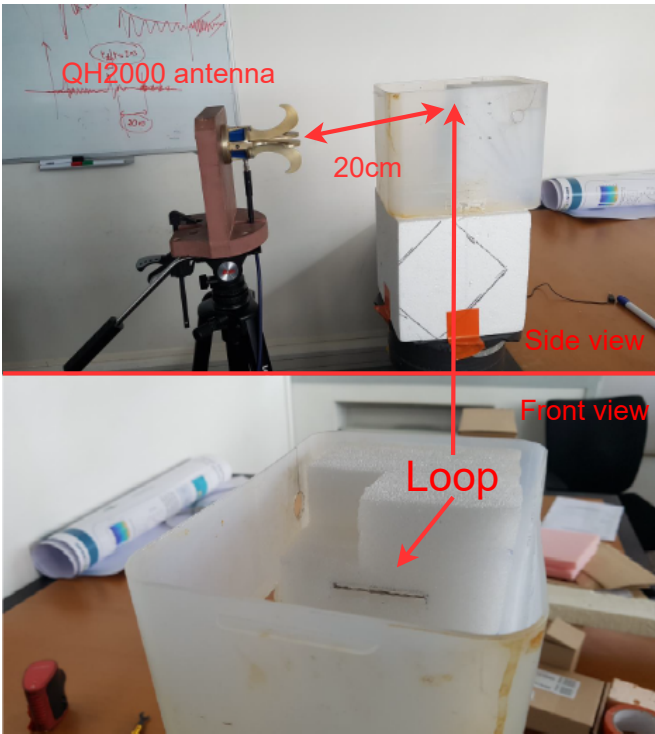


Fig. 22. Test bench configuration for the mono-static measurement in an office through a plastic box.

were recorded. Also, the measurement is done in a real environment with the presence of humans nearby as well as scattering objects (humans hand, credit card, ...). No alignment (such as calibration measurements) between the antenna and the resonator is performed, the user just place its card above the antenna. We can see that the estimated angle (given in the top of the left window) is in good agreement with the movement of the user.

A second video was recorded [27] in a bi-static configuration (see Fig. 25b), where both the elevation and azimuth angles are extracted see (26a) and (26b)]. The setup configuration is the same as before except the use of two antennas (QH2000)

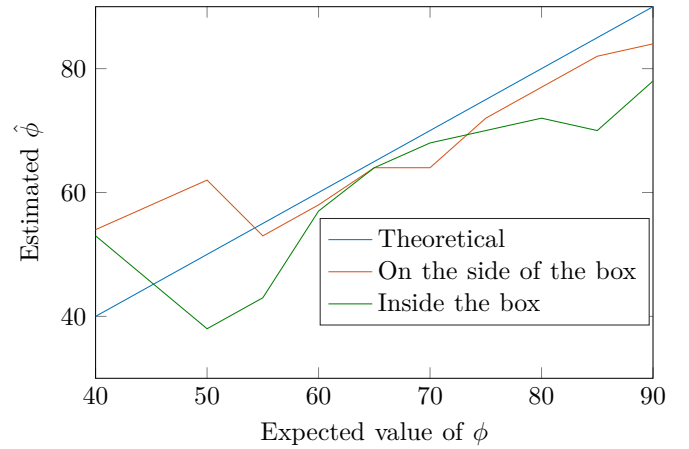


Fig. 23. Estimated value of ϕ when the resonator is placed inside a plastic box or on its side. The measurement bench is shown Fig. 22. The loop to antenna distance is 20 cm. The antenna is the QH2000 from MVG [21].

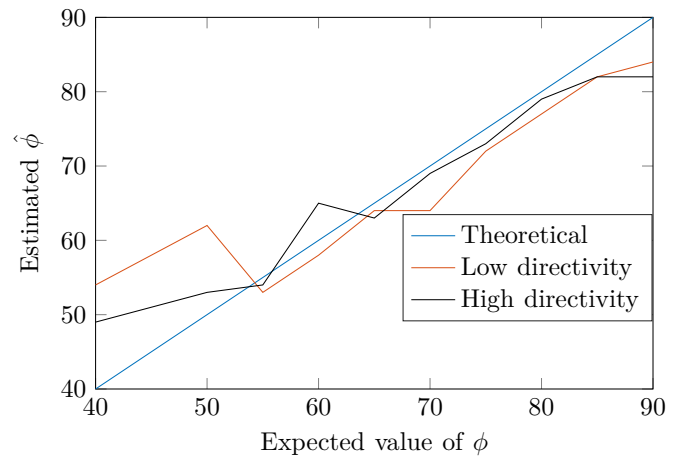


Fig. 24. Estimated value of ϕ when the resonator is placed on the side of the plastic box for a low or high directivity antenna (respectively QH2000 and QH800 from MVG [21]). The measurement bench is shown Fig. 22. The loop to antenna distance is 20 cm.

here. Due to the presence of the human and his hand near the resonator, it is not possible to obtain displacements as regular as those obtained in the monostatic configuration. However, it is possible to detect different positions of the tag. In the video, we can see that the user switches the card between two positions and the estimated angles relating to these positions are correctly detected.

Note that these two examples were recorded in real time using a computer with normal specifications. We can see that the real environment as well as the human or hand/card presence does not affect too much the sensing. In the end, the detection is compatible with this type of application. We also notice that in our case, no 'artificial intelligence', 'learning algorithm' is necessary since the resolution is done analytically on the basis of perfectly determined physical quantities. This allows us to reduce the computational cost as much as possible and to be able to present angular tracking results in real time without any specific work. A few examples of practical applications can be found in of the field of wireless joystick, human-computer

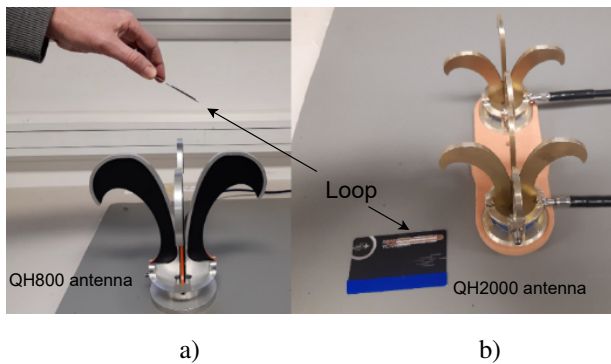


Fig. 25. Real time application: example of angular tracking. Above the reader, a user holds the resonator attached to a plastic card. Equation (23) is used to extract the angles from the measurements done by the VNA which is connected to the antennas. The result is displayed in real time on the computer screen to visualize the displacements generated by the user. a) Mono-static configuration, azimuth angle detection only, b) bi-static configuration, elevation and azimuth detection.

interface, or for gesture recognition. Indeed, the main interest here is the possibility to detect without any electronic device (obviously without battery) the angular displacement of a small object (that can also be identified) that a user would move to interact with an electronic equipment, and this at short distance. This approach based on a sensor without chip literally breaks with the solutions currently proposed which in the vast majority requires a battery to operate. This work is therefore in line with the idea of providing innovative solutions that are environmentally friendly while providing a much sought-after functionality in many applications. More precisely, we can quote for example a use to make gaming, sign language, virtual manipulation, daily assistance, or even human robot interaction.

VII. CONCLUSION

In this paper, a model of the radiating pattern of a loop resonator has been developed. This radiation pattern was then used to determine the orientation of the loop with respect to the positions of the antennas. Simulations and measurements have been done to validate the proposed method and the derived expressions. Moreover, the analytical expressions are not sensitive to the distance variation between the tag and the antennas nor to the geometry of the loop. It can be applied without indication on the distance resonator-antennas but depending on the SNR in practice, the measuring range can be reduced. Monte-Carlo simulations can be performed to estimate the measuring range knowing the SNR of the environment. Unlike chipless approaches which at best can extract a unique rotation angle, the introduced method does not require any special calibration measurements. Finally, the identification functionality of the tag (for example if we consider a tag composed by several loops similar to the one presented here) can be remained untouched so that identification and sensing can be combined to address a new kind of applications.

ACKNOWLEDGMENT

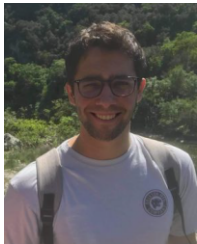
This project has received funding from the European Research Council (ERC) under the European Union's Horizon

2020 research and innovation program (grant agreement No 772539). This work is also supported by Univ. Grenoble Alpes. The authors are also thankful towards Nathalie Franck for her help in proofreading the paper.

REFERENCES

- [1] A. A. N. Shirehjini, A. Yassine, and S. Shirmohammadi, "An RFID-based position and orientation measurement system for mobile objects in intelligent environments," *IEEE Transactions on Instrumentation and Measurement*, vol. 61, no. 6, pp. 1664–1675, 2012.
- [2] H. Wang, S. Sen, A. Elgohary, M. Farid, M. Youssef, and R. R. Choudhury, "No need to war-drive: Unsupervised indoor localization," in *Proceedings of the 10th international conference on Mobile systems, applications, and services*, 2012, pp. 197–210.
- [3] S. Agrawal, I. Constandache, S. Gaonkar, R. Roy Choudhury, K. Caves, and F. DeRuyter, "Using mobile phones to write in air," in *Proceedings of the 9th international conference on Mobile systems, applications, and services*, 2011, pp. 15–28.
- [4] C. Jiang, Y. He, X. Zheng, and Y. Liu, "Orientation-aware RFID tracking with centimeter-level accuracy," in *2018 17th ACM/IEEE International Conference on Information Processing in Sensor Networks (IPSN)*. IEEE, 2018, pp. 290–301.
- [5] T. Wei and X. Zhang, "Gyro in the air: tracking 3d orientation of battery-less internet-of-things," in *Proceedings of the 22nd Annual International Conference on Mobile Computing and Networking*, 2016, pp. 55–68.
- [6] E. Perret, *Radio frequency identification and sensors: from RFID to chipless RFID*. John Wiley & Sons, 2014.
- [7] A. Ramos, E. Perret, O. Rance, S. Tedjini, A. Lázaro, and D. Girbau, "Temporal separation detection for chipless depolarizing frequency-coded RFID," *IEEE Transactions on microwave theory and techniques*, vol. 64, no. 7, pp. 2326–2337, 2016.
- [8] E. M. Amin and N. Karmakar, "Development of a chipless RFID temperature sensor using cascaded spiral resonators," in *SENSORS*, 2011, pp. 554–557.
- [9] R. S. Nair, E. Perret, S. Tedjini, and T. Baron, "A group-delay-based chipless RFID humidity tag sensor using silicon nanowires," *IEEE Antennas Wireless Propag. Lett.*, vol. 12, pp. 729–732, 2013.
- [10] C. Occhiuzzi, A. Rida, G. Marrocco, and M. Tentzeris, "RFID passive gas sensor integrating carbon nanotubes," *IEEE Trans. Microw. Theory Techn.*, vol. 59, no. 10, pp. 2674–2684, 2011.
- [11] F. Costa, A. Gentile, S. Genovesi, L. Buoncristiani, A. Lazaro, R. Villarino, and D. Girbau, "A depolarizing chipless RF label for dielectric permittivity sensing," *IEEE Microw. Wireless Compon. Lett.*, vol. 28, no. 5, pp. 371–373, 2018.
- [12] Y. Qin, Y. Fan, X. Liu, and M. M. Tentzeris, "A novel passive chipless RFID tag for angle sensor," in *2019 International Conference on Microwave and Millimeter Wave Technology (ICMMT)*, 2019, pp. 1–3.
- [13] A. Vena, E. Perret, and S. Tedjini, "A compact chipless RFID tag using polarization diversity for encoding and sensing," in *2012 IEEE International Conference on RFID (RFID)*, April 2012, pp. 191–197.
- [14] S. Genovesi, F. Costa, M. Borgese, F. A. Dicandia, A. Monorchio, and G. Manara, "Chipless RFID sensor for rotation monitoring," in *2017 IEEE International Conference on RFID Technology Application (RFID-TA)*, Sept. 2017, pp. 233–236.
- [15] S. Genovesi, F. Costa, M. Borgese, A. Monorchio, and G. Manara, "Chipless RFID tag exploiting cross-polarization for angular rotation sensing," in *2016 IEEE International Conference on Wireless for Space and Extreme Environments (WiSEE)*, Sept. 2016, pp. 158–160.
- [16] S. Genovesi, F. Costa, M. Borgese, F. A. Dicandia, and G. Manara, "Chipless radio frequency identification (RFID) sensor for angular rotation monitoring," *Technologies*, vol. 6, no. 3, 2018.
- [17] N. Barbot, O. Rance, and E. Perret, "Angle sensor based on chipless RFID tag," *IEEE Antennas Wireless Propag. Lett.*, vol. 19, no. 2, pp. 233–237, 2020.
- [18] P.-Y. Lyu, C.-C. Chang, and S.-F. Chang, "Detecting yaw and pitch change with single millimeter-wave CW radar," *IEEE Sensors Letters*, vol. 5, no. 8, pp. 1–4, 2021.
- [19] O. Rance, R. Siragusa, P. Lemaître-Auger, and E. Perret, "Contactless characterization of coplanar stripline discontinuities by RCS measurement," *IEEE Trans. Antennas Propag.*, vol. 65, no. 1, pp. 251–257, 2016.
- [20] C. A. Balanis, *Antenna theory: analysis and design*. John Wiley & Sons, 2016.

- [21] Datasheet - open boundary quad-ridge horns. MVG (2019). [accessed sep. 20, 2021.]. [Online]. Available: https://www.mvg-world.com/sites/default/files/2021-04/Datasheet_Antennas_Open%20Boundary%20Quad-Ridge%20Horns.04.21_BD.pdf
- [22] A. Ramos, E. Perret, O. Rance, S. Tedjini, A. Lázaro, and D. Girbau, "Temporal separation detection for chipless depolarizing frequency-coded rfid," *IEEE Transactions on microwave theory and techniques*, vol. 64, no. 7, pp. 2326–2337, 2016.
- [23] W. Wiesbeck and D. Kahny, "Single reference, three target calibration and error correction for monostatic, polarimetric free space measurements," *Proceedings of the IEEE*, vol. 79, no. 10, pp. 1551–1558, 1991.
- [24] P. V. Nikitin and K. S. Rao, "Theory and measurement of backscattering from rfid tags," *IEEE Antennas and Propagation Magazine*, vol. 48, no. 6, pp. 212–218, 2006.
- [25] N. Barbot, O. Rance, and E. Perret, "Classical RFID versus chipless RFID read range: Is linearity a friend or a foe?" *IEEE Trans. Microw. Theory Tech.*, 2021.
- [26] Video : real-time angle sensing using a chipless RFID resonator. [accessed 19 jan. 2022]. [Online]. Available: <https://bit.ly/3fYmQy>
- [27] Video : real-time angle sensing using a chipless RFID resonator in 3D. [accessed 19 jan. 2022]. [Online]. Available: <https://bit.ly/3tGMwPh>



Florian Requena received the M.Sc. degree in electrical engineering from the Institut National Polytechnique de Grenoble, Valence, France, in 2019. He is currently a PhD student with the Institut National Polytechnique de Grenoble at the LCIS laboratory. His current scientific interests include chipless RFID and RF sensors.



Nicolas Barbot received the M.Sc. degree and Ph.D. degree from the Université de Limoges, France. His Ph.D. work in Xlim laboratory was focused on error-correcting codes for the optical wireless channel. He also realized a post-doctoral work in joint source-channel decoding at the LSS laboratory, in Gif-sur-Yvette, France. Since September 2014, he has been an Assistant Professor at the Université Grenoble Alpes - Grenoble Institute of Technology, in Valence, France. His research interest at LCIS laboratory

includes backscattering communications, RFID and Chipless RFID. More recently, he investigates the use of chipless tag as low-cost, batteryless and robust sensors.



Darine Kaddour (Member, IEEE) was born in Mechmech, Lebanon, in February 1982. She received the B.S. degree in physics from the Faculty of Sciences, Lebanese University, Tripoli, Lebanon, in 2003, and the M.S. and Ph.D. degrees from the Institut National Polytechnique de Grenoble, Grenoble, France, in 2004 and 2007, respectively. Since 2009, she has been an Assistant Professor with LCIS, where her research includes microwave circuits and RFID antennas.



Etienne Perret (S'02–M'06–SM'13) received the Eng. Dipl. degree in electrical engineering from the Ecole Nationale Supérieure d'Electronique, d'Electrotechnique, d'Informatique, d'Hydraulique, et des Télécommunications, Toulouse, France, 2002, and the M.Sc. and Ph.D. degrees in electrical engineering from the Toulouse Institute of Technology, Toulouse, in 2002 and 2005, respectively. From 2005 to 2006, he held a post-doctoral position with the Institute of Fundamental Electronics, Orsay, France. In 2006, he was appointed Associate Professor of electrical engineering at Grenoble INP - Institute of Engineering Univ. Grenoble Alpes, France. From 2014 to 2019, he has been a Junior Member with the Institut Universitaire de France, Paris, France, an institution that distinguishes professors for their research excellence, as evidenced by their international recognition. From 2015 to 2020, he has been an Appointed Member of the French National Council of Universities. He has authored or co-authored more than 200 technical conferences, letters and journal papers, and books and book chapters. He holds several patents. His works have generated more than 3300 citations. His current research interests include electromagnetic modeling of passive devices for millimeter and submillimeter-wave applications, and wireless communications, especially RFID and chipless RFID, and also include advanced computer-aided design techniques based on the development of an automated codesign synthesis computational approach. Dr. Perret is a Technical Program Committee member of the IEEE International Conference on RFID, the IEEE RFID TA; and a member of the IMS Technical Paper Review Committee. He was a recipient of several awards like the MIT Technology Review's French Innovator's under 35 in 2013, the French Innovative Techniques for the Environment Award in 2013, the SEE/IEEE Leon Brillouin Award for his outstanding achievement in the identification of an object in an unknown environment using a chipless label or tag in 2016, the IEEE MTT-S 2019 Outstanding Young Engineer Award and the Prix Espoir IMT – Académie des sciences in 2020. He was a Keynote Speaker and the Chairman of several international symposiums. Etienne Perret was awarded an ERC Consolidator Grant in 2017 for his project ScattererID.